Contents lists available at ScienceDirect

Nano-Structures & Nano-Objects

Copper-doped zinc tartrate (Cu-ZnT) nanocrystals: Exploring their physical and antimicrobial properties

Charushila Pawar [a,*], Madhuri Patil [b]

[a] Department of Chemistry, M. V. P'S Arts, Science, and Commerce College. Ozar (Mig), Nashik, Maharashtra 422207, India
[b] Department of Chemistry, J. D. M. V. P Nutan Maratha College, Jalgaon, Maharashtra 425001, India

ABSTRACT

This study investigates the growth and properties of pure zinc tartrate (ZnT) and copper-doped zinc tartrate (Cu-ZnT) nanocrystals synthesized via a sol-gel technique using double-distilled water, sodium metasilicate, and tartaric acid. Controlled pH gels were prepared with the subsequent addition of zinc chloride and copper chloride solutions to facilitate nanocrystal formation. The synthesized nanocrystals were characterized using various techniques, including Energy-Dispersive X-ray analysis, Fourier Transform Infrared Spectroscopy, Thermogravimetric analysis, UV–visible-near infrared spectral analysis, X-ray diffraction (XRD), and Field Emission Scanning Electron Microscopy. EDAX confirmed the elemental composition of Zn, Cu, C, and O in the crystals. FTIR spectra revealed the presence of functional groups corresponding to water of crystallization, tartaric acid moieties, and potentially other compounds. TGA analysis indicated a two-stage decomposition process for ZnT and the formation of zinc copper oxide in Cu-ZnT. UV–vis-NIR analysis yielded a low cut-off wavelength of 285 nm for both crystals, suggesting electronic transitions below 350 nm. Both ZnT and Cu-ZnT nanocrystals are transparent in visible and near-infrared light, absorbing strongly in the ultraviolet. Copper doping enhances Cu-ZnT light absorption. While both act as insulators, Cu-ZnT exhibits significantly higher conductivity due to copper doping. XRD analysis estimated an average crystalline size of 42 nm, while FE-SEM images revealed a quasi-spherical morphology. Refractive index, extinction coefficient, and optical bandgap were further determined, highlighting the potential suitability of these nanocrystals for optoelectronic applications. Antibacterial and antifungal assays demonstrated moderate effectiveness against tested microorganisms compared to standard drugs.

1. Introduction

The nanocrystals are essential to modern research and technology because of their distinct features, which are determined by their physical characteristics such as atomic organization, packing, and composition, and promising in biosensing, catalysis, and optoelectronics applications [1]. The initial and most significant phase towards understanding the structure and possible uses of any nanocrystal is to produce crystals of appropriate size and packing. Metal tartrate compounds have been the focus of significant research due to their diverse properties and wide applications [2]. The growth of nanocrystals using gel-based techniques has gained significant attention among researchers. This method is especially beneficial for the development of doped crystals, which have potential industrial and practical applications. Solution gel growth, an early crystal growth technique, has regained significance for compounds such as tartrate acids. Because these chemicals tend to break down before reaching boiling point and have limited water solubility, conventional methods are less effective. As such, gel-based approaches have emerged as the preferred method for successful crystal growth and development [3]. The transition metal ions such as Cu, Mn, and Co can be incorporated into the matrix to produce new materials with interesting and unique properties. Zinc tartrate (ZnT) is a versatile material with intriguing properties that hold promise for various applications. This section is divided into the specific characteristics of ZnT across different domains. Limited information exists regarding ZnT thermal behavior. However, studies suggest it decomposes at around 399.3 °C. Exploring its thermal stability further could the way for applications in heat-resistant materials. ZnT exhibits phosphorescence, the ability to emit light after absorbing energy. This characteristic has potential applications in light-emitting devices and luminescent materials [4].

Further research on its photoluminescence properties could unlock its full potential in optoelectronics. While the detailed electrical conductivity of ZnT remains uninvestigated, its potential as a synergist in cosmetics suggests interactions with electrical charges in the skin. Understanding its electrical properties could lead to innovative cosmetic formulations. Recent research indicates the potential antimicrobial activity of ZnT against certain gram-positive bacteria. Exploring this aspect further could lead to applications in antibacterial coatings and hygiene products [5]. Copper doping, known to significantly influence superconductivity, photocatalytic activity, electrical behavior, and optical properties in various materials, presents a fascinating avenue for enhancing ZnT functionalities. This study aims to bridge the knowledge gap by investigating the impact of copper doping on ZnT nanocrystals synthesized using the gel technique [6]. The characterization process will utilize advanced analytical techniques such as Energy-Dispersive X-ray spectroscopy, Thermogravimetric analysis, Fourier Transform Infrared spectroscopy, UV–visible spectroscopy, X-ray diffraction, and Field Emission Scanning Electron Microscopy. These techniques will provide valuable insights into the elemental composition, thermal stability, functional groups, optical properties, crystal structure, and morphology of the synthesized nanocrystals [7]. To complement the comprehensive characterization techniques outlined above, this study will also investigate the potential antimicrobial properties of the synthesized nanocrystals [8,9]. The research by El Nahrawy et al. (2021) contributes to the growing body of knowledge on doped ZnTiO3 nanocrystals. Prior studies have explored how different dopant elements influence the properties of these materials [10]. For instance, Bakr et al. (2021) investigated the effects of aluminum (Al), iron (Fe), and copper (Cu) on the microstructure, diffused reflectance, terahertz response, and dielectric properties of ZnTiO3 nanocrystals [11]. Their work provides a valuable reference point for understanding how Cu doping specifically affects Cu-ZnTiO3 compared to the influence of other dopant elements. Furthermore, El Nahrawy et al. (2019) examined the thermal, dielectric, and antimicrobial properties of nanocomposites that combine copper with other materials. In their study, polystyrene and copper were incorporated into indium tin oxide (ITO) [12]. This research highlights the potential functionalities of copper in nanomaterials. By drawing connections to this earlier work, El Nahrawy et al. can offer insights into how Cu might contribute to the properties of Cu-ZnTiO3 nanocrystals beyond the immediate scope of their current investigation [13]. This additional facet will offer valuable insights into the broader applicability of these materials. The present research holds significant promise for advancing our knowledge of copper-doped ZnT nanocrystals. By elucidating the structure-property relationships and exploring their potential antimicrobial activity, this work provides the way for their future applications in optoelectronics and potentially in the field of antibacterial materials [14,15].

2. Materials and methods

2.1. Materials

Double-distilled water (Milli-Q or equivalent, 18.2 MΩ.cm resistivity), Whatman filter paper (Grade 1 qualitative filter paper), Sodium metasilicate (Na_2SiO_3), high purity ($\geq$ 99 %), L-(+)-Tartaric acid ($C_4H_6O_6$), high purity ($\geq$ 99.5 %), Zinc chloride ($ZnCl_2$), analytical grade ($\geq$ 99.0 %), Copper chloride dihydrate ($CuCl_2.2\,H_2O$), analytical grade ($\geq$ 99.0 %)

2.2. Method

This study employed the gel technique for the synthesis of ZnT and Cu-ZnT nanocrystals. High-purity double-distilled water (Milli-Q or equivalent, resistivity $\geq$ 18.2 MΩ cm) was used throughout the experiment to minimize impurities. The water was further filtered using Whatman filter paper for additional purification. Separate solutions of

1 M sodium metasilicate (Na_2SiO_3, $\geq$ 99 % purity) and 1 M L-(+)-tartaric acid ($C_4H_6O_6$, $\geq$ 99.5 % purity) were prepared in the double-distilled water. To create the gel, the sodium metasilicate solution was gradually added to the tartaric acid solution under continuous magnetic stirring. A pH meter was used to monitor the solution, and the addition of sodium metasilicate was stopped when the pH reached 5.0 to ensure controlled gelation [16,17]. Continuous stirring throughout this process prevented localized high concentrations of ions, promoting uniform gel formation. The prepared gel was then carefully poured into clean test tubes to avoid air bubbles. Cotton wool was used to cover the test tubes, preventing dust contamination and minimizing solvent evaporation. The gel was allowed to set undisturbed at room temperature for 24–48 hours. Following complete gelation, the appropriate metal chloride solution (1 M $ZnCl_2$ for ZnT or 0.5 M $CuCl_2.2\,H_2O$ for Cu-ZnT) was gently layered on top of the gel using a pipette to minimize disruption. The test tubes were then sealed and placed stationary at room temperature to initiate crystal growth. Crystal formation was typically observed within a week, with nanocrystals reaching their maximum size within approximately one month [18].

2.3. Antibacterial and antifungal study

The effectiveness of the synthesized ZnT and Cu-ZnT nanocrystals against bacteria and fungi was evaluated using the agar diffusion method. Specific bacterial and fungal strains were selected for the study. These organisms were first cultured in nutrient broth for 18 hours at 37 °C to achieve a standardized inoculum density. Meanwhile, Mueller-Hinton agar plates were prepared according to the manufacturer's instructions. The agar diffusion assay involved creating wells of a defined diameter (6 mm) using a sterile cork borer in the prepared agar plates. Known volumes (10 µL) of test solutions, prepared by dissolving the synthesized crystals in a specified solvent at a specific concentration, were then pipetted into each well. To compare the effectiveness of the test crystals against bacteria, a well containing a standard antibiotic solution (Streptomycin, Gentamycin) was included as a positive control. Similarly, wells containing standard antifungal solutions (Itraconazole, Fluconazole) were incorporated as positive controls for the antifungal activity test. After inoculation, the agar plates were incubated at 37 °C for bacteria or at appropriate conditions specific to the chosen fungal strains. Following incubation, the diameter of the clear zone of inhibition surrounding each well containing the test solution, standard antibiotic/antifungal control, was measured. This data was used to calculate the mean zone of inhibition for each test organism and treatment group [19] [20]. By analyzing these results, the antimicrobial and antifungal activity of the synthesized nanocrystals could be compared to the standard controls. This comparison would allow for the evaluation of ZnT and Cu-ZnT effectiveness against various bacteria and fungi relative to established antibiotics and antifungals.

3. Result and discussion

3.1. UV–Vis–NIR spectral analysis

The optical properties of the synthesized ZnT and Cu-ZnT nanocrystals were investigated using UV–visible (UV-Vis) spectroscopy. The absorption spectra were recorded in the wavelength range of 200–800 nm with a Jasco Spectrophotometer. Both ZnT and Cu-ZnT nanocrystals displayed a low cut-off wavelength of approximately 285 nm. However, ZnT exhibited a superior transparency of around 96 % at this wavelength compared to Cu-ZnT with a transparency of 86 %. This suggests a stronger absorption of light below 285 nm in Cu-ZnT nanocrystals [21,22]. In both cases, the observed absorption below 350 nm is attributed to electronic transitions within the material.

3.1.1. Optical Bandgap
ZnT nanocrystals exhibited a wider optical transmission window,

reaching a transparency of approximately 96 %. This high transparency makes ZnT a promising candidate for nonlinear optical (NLO) applications, where efficient light transmission is crucial [23]. The origin of the slight peak observed near 400 nm in Fig. 1(a) is under investigation and further studies are required to determine its exact nature. It is unlikely to be a Cu plasmon peak signal as these are typically located within the near-infrared (NIR) region, while Cu, Au, and Ag plasmons are generally found in the blue-visible spectral range. The wide bandgap further emphasizes the potential suitability of ZnT for optoelectronic device applications [24,25].

3.1.2. Impact of copper doping

Cu-doped ZnT nanocrystals displayed an estimated optical bandgap of 3.41 eV, which closely aligns with the experimentally determined bandgap of 3.60 eV obtained from the UV-Vis spectra (fig. 1(b)). This observation suggests that copper doping influences the electronic structure of ZnT, potentially leading to a slight decrease in the bandgap energy. Copper doping in Cu-ZnT nanocrystals introduces new energy levels within the bandgap, including shallow acceptor levels from Cu substituting Zn and potentially d-d electron transitions. These levels can influence electrical conductivity by increasing p-type character through additional hole carriers, though scattering effects from dopants can also play a role. Techniques like Hall effect measurements and temperature-dependent conductivity studies can provide further insights into the electrical property modifications caused by copper doping. Nevertheless, the wide energy gap exhibited by Cu-ZnT remains highly favorable for photovoltaic applications, where efficient light absorption across a broad solar spectrum is desired [26,27].

3.1.3. Extinction coefficient and refractive index

The extinction coefficient (K) and refractive index (n) of both ZnT and Cu-ZnT nanocrystals were measured across a specific wavelength range. The refractive index exhibited minimal variation throughout the investigated wavelength range (320–850 nm) for both crystals (fig. 2(a) and (b)). This suggests minimal dispersion within this spectral window.

The minimal variation of refractive index (n) across a broad wavelength range (320–850 nm) in Cu-ZnT nanocrystals suggests a material with constant phase velocity for light propagation, a desirable property for optoelectronic applications. This constant refractive index translates to minimal dispersion, ensuring minimal signal distortion in optical waveguides and enabling sharp filters by allowing precise control of light propagation within a specific wavelength range (fig. 2(b)). These properties make Cu-ZnT nanocrystals promising candidates for various optoelectronic devices.
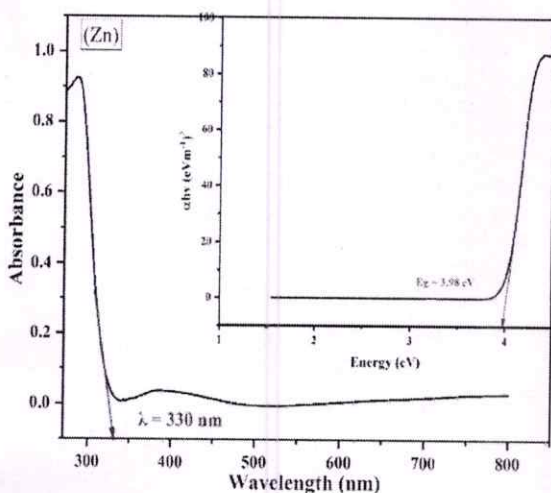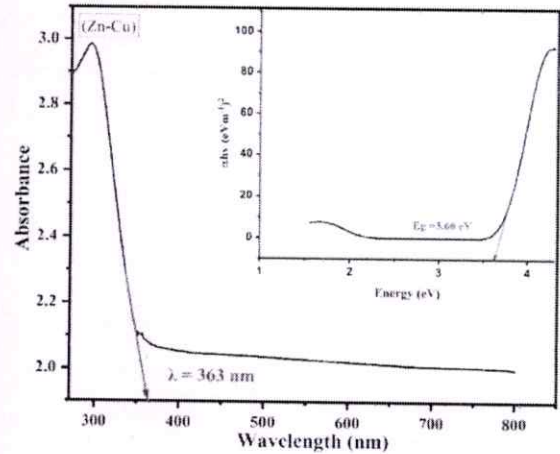

Fig. 1(b). Absorbance vs wavelength (nm) of Cu-ZnT nanocrystal.

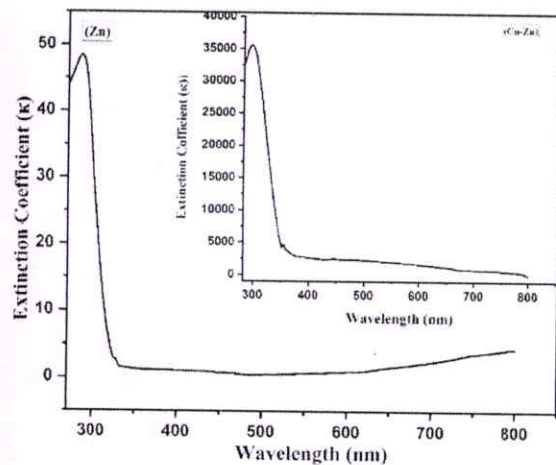**Fig. 2(a).** The curve of Extinction coefficient (k) vs. wavelength (nm) of ZnT and Cu-ZnT nanocrystals.
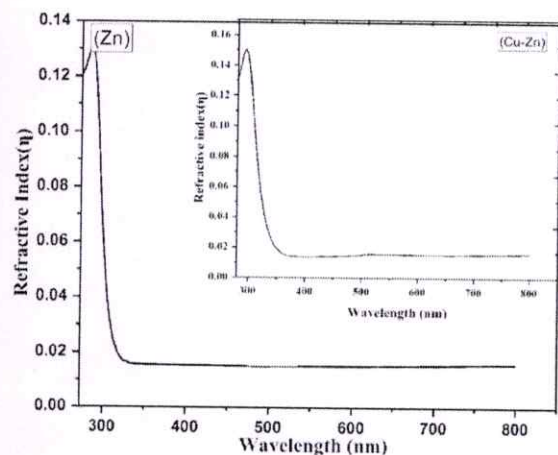

Fig. 2(b). The refractive index (η) vs. wavelength (nm) of ZnT and Cu-ZnT nanocrystals.

3.1.4. Absorption and transmittance

An interesting characteristic observed was the linear relationship between transmittance (T) and wavelength for both ZnT and Cu-ZnT
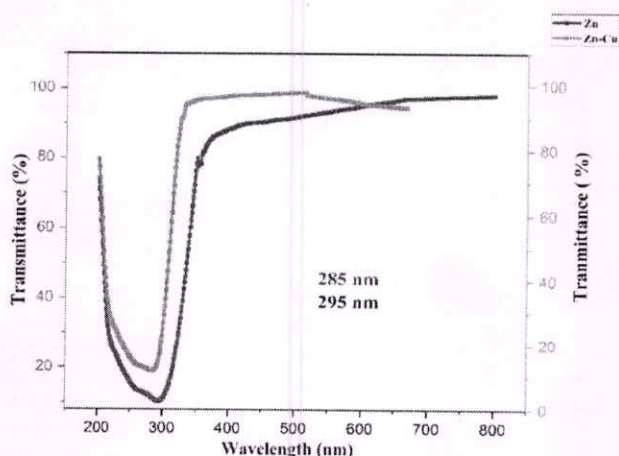

Fig. 1(a). Absorbance vs wavelength (nm) of ZnT nanocrystals.

Fig. 3. Transmittance (%) vs wavelength (nm) of ZnT and Cu-ZnT nanocrystals.

(Fig. 3). This finding emphasizes the critical role of reflection (R) in determining the overall optical properties of these materials. The relationship between these parameters can be expressed by the equation: T = 1 - Kd - R, where d is the thickness of the sample. Optimizing both absorption and reflection becomes crucial for designing efficient optical devices [28].

The linear relationship between transmittance (T) and wavelength in Cu-ZnT nanocrystals affirms the Lambert-Beer Law and signifies minimal scattering losses. This linearity accentuates the critical role of reflection (R) since any decrease in T can be attributed to the combined effects of Kd and R. Therefore, for efficient optoelectronic devices utilizing Cu-ZnT nanocrystals, optimizing both absorption and reflection becomes essential for achieving desired light management.

3.1.5. Comparison of crystal properties

ZnT nanocrystals displayed superior transparency (around 96 %) compared to Cu-ZnT (around 86 %) at a specific wavelength. Despite this difference, both crystals exhibit promising optical characteristics for diverse applications. The bandgap values, determined through appropriate methods showed slight variations between the two materials. However, the wide bandgaps observed in both ZnT and Cu-ZnT suggest their potential applicability in optoelectronic devices.

3.1.6. Reflectance

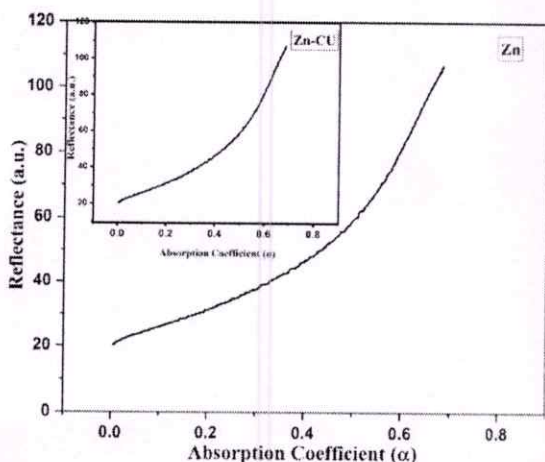The linear relationship between reflectance and the absorption

Fig. 4. Reflectance (a.u) vs absorption coefficient (α) of ZnT and Cu-ZnT nanocrystals.

coefficient observed in Fig. 4 highlights the importance of considering both parameters simultaneously during material optimization. This is because reflectance (R) and absorbance (A) are related through the equation R + A + T = 1, where T is the transmittance. Here, T represents the portion of light that passes through the material. By manipulating the absorption coefficient (which influences A) and reflectance, researchers can achieve the desired level of light transmission or absorption within the material. This control over the overall optical response allows for tailoring materials for specific optoelectronic applications. This concept aligns with previous research findings in the field of thin-film optics, where optimizing both absorption and reflectance is crucial for devices like antireflection coatings and optical filters [29] [30].

3.2. FTIR analysis

FTIR spectroscopy was employed to analyze the functional groups present in both ZnT and Cu-ZnT nanocrystals. For ZnT nanocrystals, a peak at 3458.71 cm^{-1} suggests the presence of hydroxyl groups (OH) or adsorbed water molecules. Another peak at 1607.38 cm^{-1} corresponds to the C=O stretching vibration of carboxylate groups (COO⁻) within the tartrate molecule. Additional peaks between 1377.89 cm^{-1} and 1112.73 cm^{-1} can be assigned to various stretching and bending vibrations of the C-O bond and other functional groups in the ZnT structure. Lower wavenumber peaks (932.414 cm^{-1} to 513.936 cm^{-1}) likely represent out-of-plane bending modes involving functional groups within the crystal lattice [31,32] (Fig. 5).

The FTIR spectrum of Cu-ZnT displayed a similar overall pattern with some differences. The peak positions for Cu-ZnT exhibited slight shifts compared to ZnT, particularly for the asymmetric and symmetric stretching vibrations of the C-O bond in the carboxylate group (Fig. 6). These shifts might indicate subtle changes in the vibrational environment due to copper doping. While some peaks remained similar to ZnT, suggesting the preservation of the core structure, the presence of copper seems to influence the bonding interactions to a certain extent.

The FTIR analysis confirmed the presence of expected functional groups associated with the tartrate molecule in both ZnT and Cu-ZnT nanocrystals. The observed peak shifts in Cu-ZnT suggest a potential influence of copper doping on the vibrational modes and local bonding environment within the crystals [33,34].

3.3. Thermal decomposition analysis (TGA)

The TGA was performed to investigate the thermal decomposition behavior of Cu-ZnT and ZnT nanocrystals. The analysis shows distinct weight loss events at specific temperature ranges, suggesting a multi-step decomposition process for both materials.

3.3.1. TGA of ZnT

ZnT also underwent a two-step decomposition process as revealed by TGA. The first weight loss, occurring between 52.90 °C and 123.40 °C, resulted in a measured loss of 19.34 %, which is very close to the calculated value of 20.03 %. Similar to Cu-ZnT, this initial weight loss is attributed to the removal of adsorbed water molecules or surface hydroxyl groups on the Zn tartrate crystals (fig. 7(a) and (b)). The close agreement between observed and calculated values suggests an efficient process for water desorption from the ZnT. The second weight-loss event, corresponding to the decomposition of the tartrate molecule within ZnT, occurred around 319.30 °C and 385.0 °C. Here, a total weight loss of 47.72 % was observed, which is reasonably close to the calculated value of 44.55 %.

This suggests a decomposition process for the organic component similar to what was observed in Cu-ZnT. However, an interesting difference is the presence of two distinct peaks in the Zn tartrate weight loss curve compared to a single broader peak for Cu-ZnT. This might indicate a slightly different pathway for the decomposition of the organic moiety
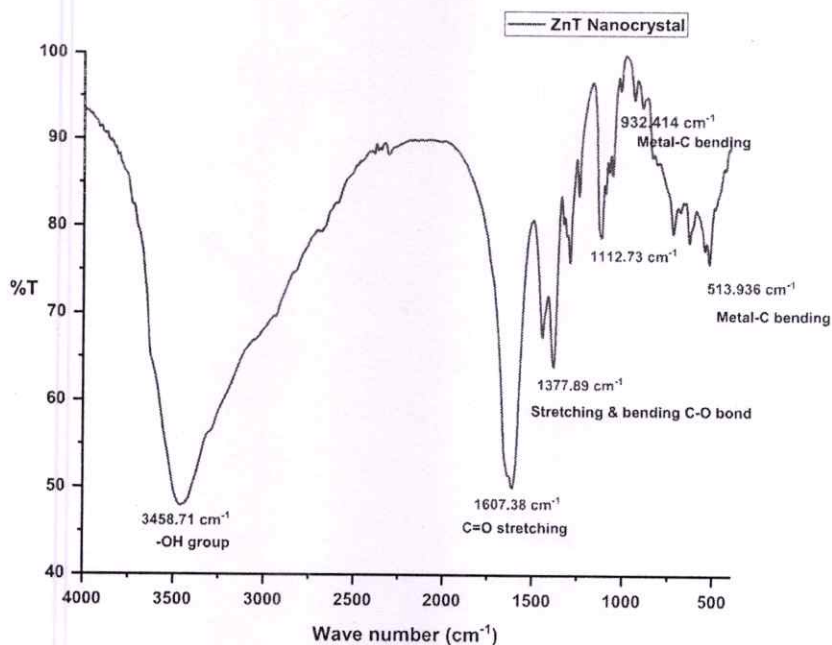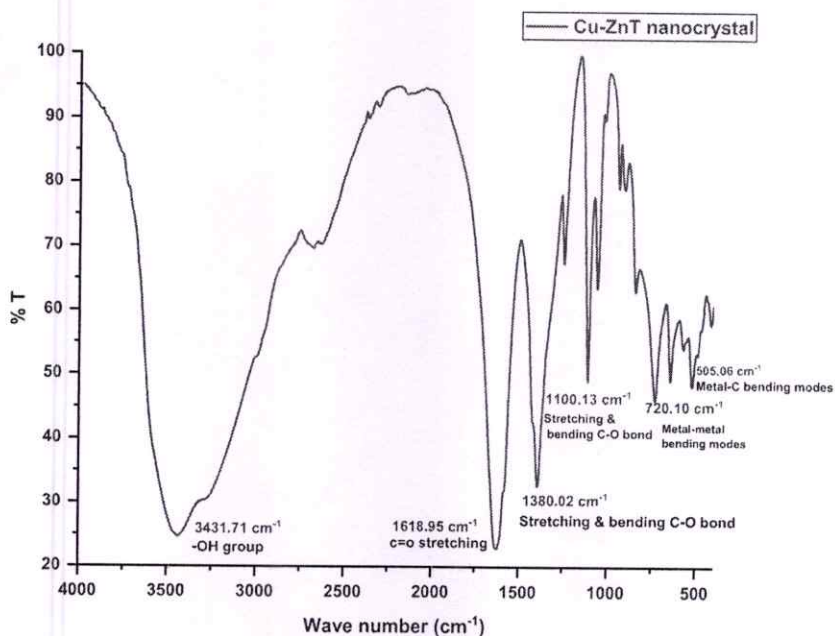
Fig. 5. FTIR spectra of ZnT nanocrystal.

Fig. 6. FTIR spectra of Cu-ZnT nanocrystals.

within Zn tartrate crystals compared to Cu-ZnT [35,36] (Table 1).

3.3.2. Cu-Doped Zn tartrate (Cu-ZnT)

The TGA provided insights into the thermal decomposition behavior of Cu-ZnT. The analysis revealed a two-stage weight loss process. The initial weight loss observed between 36.06 °C and 64.95 °C with a measured loss of 7.5 %, is likely due to the removal of water molecules or hydroxyl groups adsorbed on the Cu-ZnT crystal surface. A slight difference between the observed and calculated value (9.8 %) could be attributed to factors like incomplete moisture removal during sample preparation or variations in the initial water content. The second, more

significant weight loss occurred between 220.05 °C and 250.68 °C. Here, a 53.01 % weight loss was observed, which closely matches the calculated value of 50.69 %. This significant decomposition is attributed to the breakdown of the organic component, most likely the tartrate moiety ($C_4H_6O_6$) within the Cu-ZnT crystals. The decomposition products likely include volatile species like carbon dioxide (CO_2), water vapor (H_2O), and potentially some organic fragments [37,38].

3.4. XRD analysis

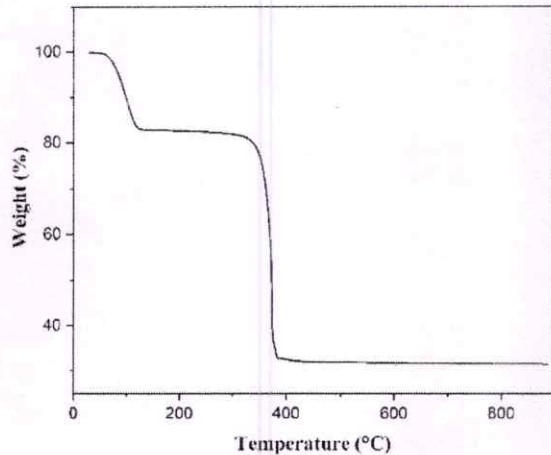XRD analysis of ZnT and Cu-ZnT nanocrystals (fig. (a) and (b)),
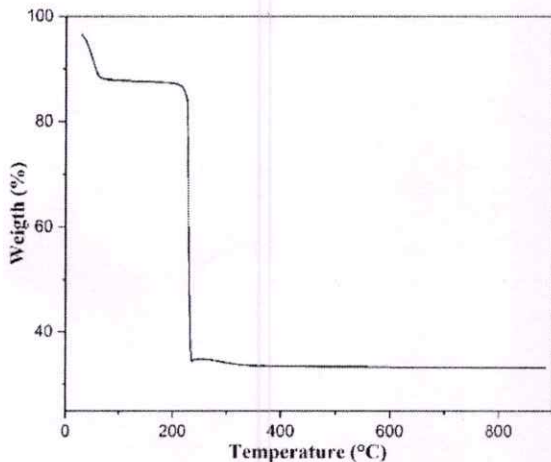
Fig. 7(a). TGA of ZnT nanocrystal.

Fig. 7(b). TGA of Cu-ZnT nanocrystal.

exhibiting an average crystallite size of 51.88 nm and 42.00 nm respectively, is expected to reveal a characteristic diffraction pattern with several distinct peaks. These peaks correspond to the constructive interference of X-rays diffracted by specific crystallographic planes within the ZnT and Cu-ZnT lattice [33]. The precise positions and relative intensities of these peaks will be dictated by the unit cell parameters and crystallographic orientation of nanocrystals. However, due to the small crystallite size (51.88 nm and 42.00 nm), the Scherrer equation predicts the broadening of these diffraction peaks compared to their counterparts in larger crystals. This broadening arises from the confinement of diffracting domains within the nano-crystallites, leading to a wider range of diffracted angles and consequently broader peaks [39]. Analysis of this peak broadening using the Scherrer equation can be a valuable tool for confirming the average crystallite size of these samples [40].

The data analysis involved interpreting the XRD pattern using the

Rietveld refinement method with FullProf Suite software. This technique allowed for a detailed analysis of the peak positions and intensities. To identify the crystal structure, the Crystallography Open Database (COD) was used, specifically the ZnT and Cu-ZnT CIF files corresponding to the P-3112 space group. The analysis confirmed the crystallinity of the ZnT and Cu-ZnT nanocrystals based on the sharp peaks in the pattern. Furthermore, the analysis revealed a trigonal crystal system with specific lattice parameters and unit cell volume. The positions of the major diffraction peaks were then assigned specific Miller indices based on their intensity. Finally, the calculated d-spacings from the proposed unit cell parameters matched well with the experimentally measured values, further supporting the structural model [41].

The Scherrer equation is $D = K\lambda / [\beta \cos(\theta)]$;

λ = X-ray wavelength (typically 1.54 Å for Cu Kα radiation),

K = Scherrer constant,

β = broadening of the diffraction peak at full width at half maximum (FWHM) in radians. This can be calculated from the measured peak width in the XRD pattern using $\beta = \beta'\pi/180$, where β' is the FWHM in degrees, θ = diffraction angle. The average crystalline size is 51.88 nm and 42.00 nm for ZnT and Cu-ZnT nanocrystals respectively.

3.5. FE-SEM and EDS analysis

The EDX analysis successfully verified the elemental composition of both ZnT and Cu-ZnT nanocrystals. The presence of the expected elements (O, C, and Zn) and the absence of copper in ZnT confirm its purity (Table 2). For Cu-ZnT, the detection of a small quantity of copper confirms the doping process. The observed weight and atomic percentages provide quantitative information about the elemental composition of these materials [42].

EDX analysis confirmed the composition of ZnT and Cu-ZnT. Pure ZnT contained mainly oxygen (O), carbon (C), and zinc (Zn), with no copper (Cu) detected. Cu-ZnT showed similar elements but with a small presence of Cu, verifying successful doping (Fig. 9).

The FE-SEM image offers a glimpse into the surface morphology of the ZnT and Cu-ZnT nanocrystals. The FE-SEM image shows a black-and-white microphotograph of a rock-like substance (Fig. 10). The overall size of the nanocrystals could potentially indicate the width of a particular structure on the ZnT surface. The image shows a non-uniform texture with both smooth and rough features. This suggests that some features within the image of ZnT and Cu-ZnT might be around 235 and 65 nanometres in size respectively.

3.6. Antimicrobial assay

The antimicrobial activity of ZnT and Cu-ZnT nanocrystals with a

Table 2
Atomic and weight percentages of the constituent elements.

Nanocrystal	Parameter	Elements			
		O	C	Cu	Zn
ZnT	Weight %	48.42	21.74	–	29.84
	Atomic %	59.06	34.52	–	6.420
Cu-ZnT	Weight %	49.02	23.43	0.21	27.34
	Atomic %	59.82	34.71	0.07	5.400

Table 1
Decomposition process ZnT and Cu-ZnT nanocrystals.

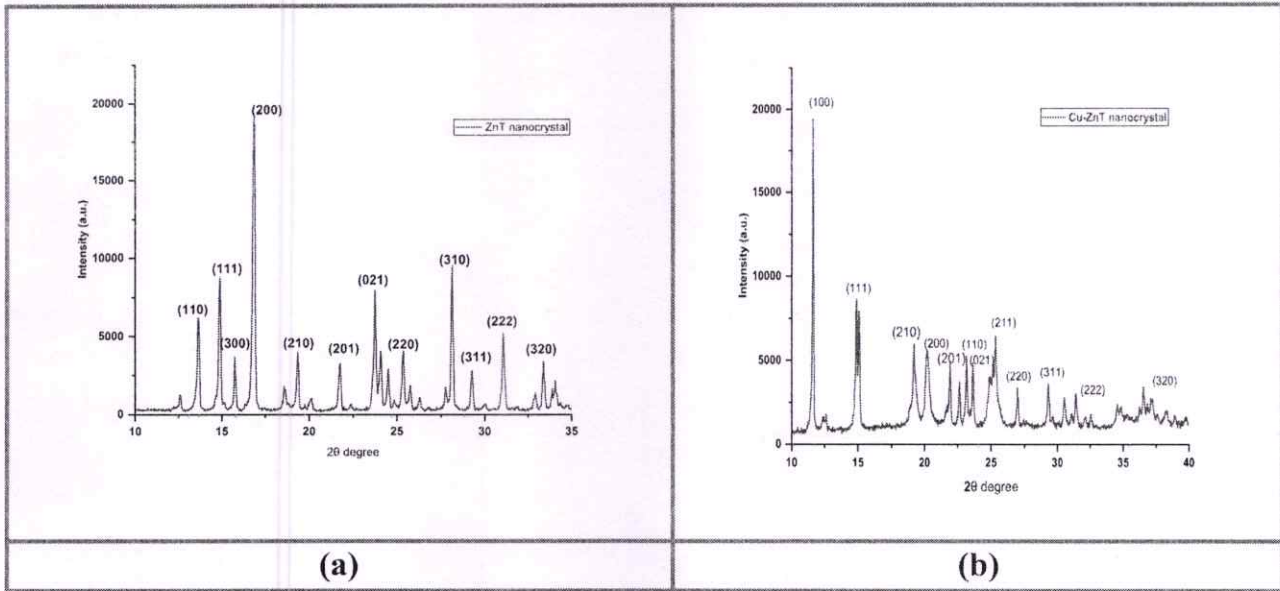| Name of the crystal	Temperature (C)	Weight loss (%)		Reaction
		Observed	Calculated	$ZnCuC_4H_4O_6.5\,H_2O \longrightarrow ZnCuC_4H_4O_6.3\,H_2O + 2\,H_2O$ $ZnCuC_4H_4O_6.3\,H_2O \longrightarrow ZnCuO + 5\,H_2O + CO_2 + CO +$
Cu-ZnT	36.060–64.950	7.500	9.800	2 C
	220.05–250.68	53.01	50.69	
ZnT	52.900–123.40	19.34	20.03	$ZnC_4H_4O_6.7\,H_2O \longrightarrow ZnC_4H_4O_6.3\,H_2O + 4\,H_2O$
	319.30 & 385.0	47.72	44.55	$ZnC_4H_4O_6.3\,H_2O \longrightarrow ZnO + 5\,H_2O + CO_2 + CO + 2\,C$

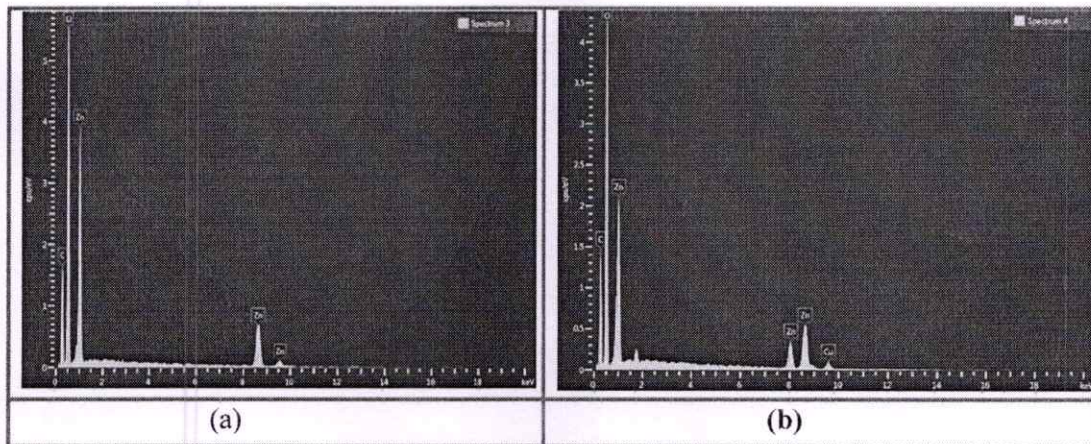**Fig. 8.** XRD of (a) ZnT and (b) Cu-ZnT nanocrystal.

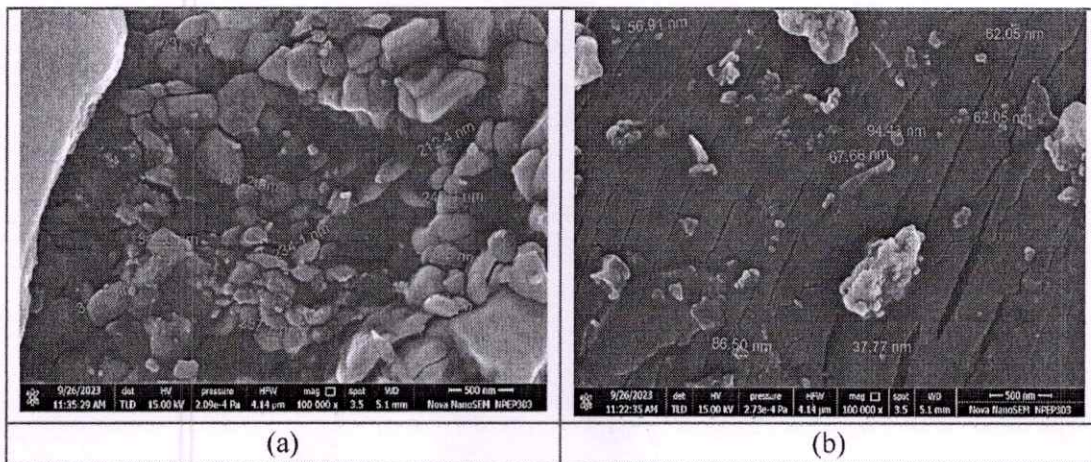**Fig. 9.** EDAX of (a) ZnT and (b) Cu-ZnT nanocrystal.

Fig. 10. FE-SEM of (a) ZnT and (b) Cu-ZnT nanocrystal.

concentration of 200 µg/ml tested against *Escherichia coli, Bacillus subtilis, Staphylococcus aureus,* and *Pseudomonas Aeruginosa* shows the following results. ZnT exhibited antimicrobial activity against *Escherichia coli,* showing a mean zone of inhibition of 15.3 mm, and against *Bacillus subtilis* with a mean zone of inhibition of 15.6 mm. Against *Pseudomonas Aeruginosa,* it showed a mean zone of inhibition of 11 mm. Cu-ZnT showed antimicrobial activity against *Escherichia coli,* with a mean zone of inhibition of 16.6 mm, and against *Bacillus subtilis* with a mean zone of inhibition of 13.3 mm. Against *Staphylococcus aureus,* the mean zone of inhibition is 12.5 mm. In comparison, the positive controls (Streptomycin and Gentamycin) showed larger zones of inhibition, indicating that the studied crystals are less effective than the positive control (Fig. 11) [40]. While ZnT and Cu-ZnT showed antimicrobial activity against the tested bacteria, their effectiveness is relatively lower than that of the standard drugs, further studies are necessary to explore the potential use of these nanocrystals as potent antimicrobial agents (Fig. 12) [43,44].

In the antifungal activity tests conducted against *Aspergillus Niger, Candida albicans, Fusarium spp.,* and *Penicillium Chrysogenum,* both ZnT and Cu-ZnT samples showed inhibitory effects.
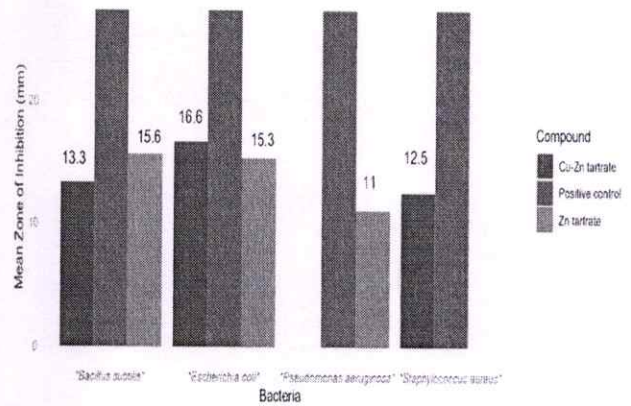

Fig. 12. A bar graph illustrating the diameter of the zone of inhibition (in mm) produced by both ZnT and Cu-ZnT nanocrystals in the presence of bacteria.
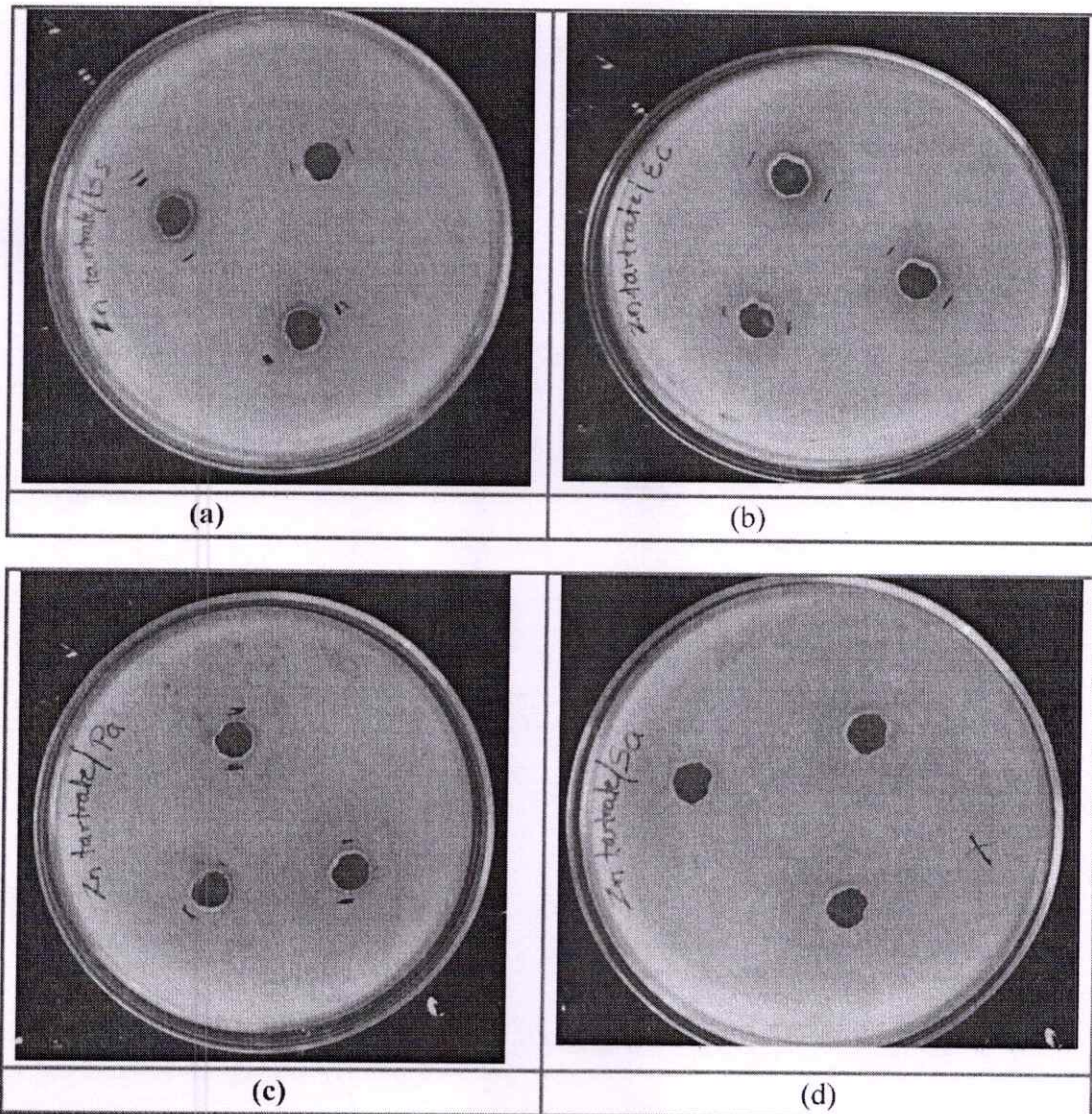

Fig. 11. The zone of inhibition (in mm) produced by both ZnT and Cu-ZnT nanocrystals in the presence of bacteria; (a) *Bacillus subtilis,* (b) *Escherichia coli,* (c) *Pseudomonas Aeruginosa,* and (d) *Staphylococcus aureus.*

ZnT demonstrated mean zones of inhibition measuring 13.5 mm and 12.6 mm against *Aspergillus Niger* and *Candida albicans*, respectively, whereas Cu-ZnT has higher effectiveness with mean zones of inhibition of 19.3 mm and 15 mm against the same microorganisms (Fig. 13).

Comparative analysis with positive controls (Itraconazole and Fluconazole) affirmed the superior inhibitory activity of the samples [39, 40]. When tested against *Fusarium spp.* and *Penicillium chrysogenum*, ZnT exhibited zones of inhibition measuring 13.3 mm and 12 mm, while Cu-ZnT showed increased effectiveness with mean zones of inhibition of 15 mm and 12.6 mm, respectively. Despite their antifungal properties, both ZnT and Cu-ZnT have lower effectiveness than the positive controls. Cu-ZnT displayed the highest effectiveness against *Aspergillus Niger* and *Fusarium spp.*, although the positive controls remained more potent in inhibiting fungal growth in both cases (Fig. 14).

4. Conclusion

This study successfully synthesized ZnT and Cu-ZnT nanocrystals using a sol-gel diffusion technique. The optimized process yielded high-quality, quasispherical nanocrystals with the desired size range. EDAX confirmed the presence of expected elements (Cu, Zn, O, C) and validated the copper doping in Cu-ZnT crystals. Thermal analysis revealed the presence of trapped water molecules within both nanocrystals. Interestingly, Cu-ZnT exhibited a lower thermal stability compared to
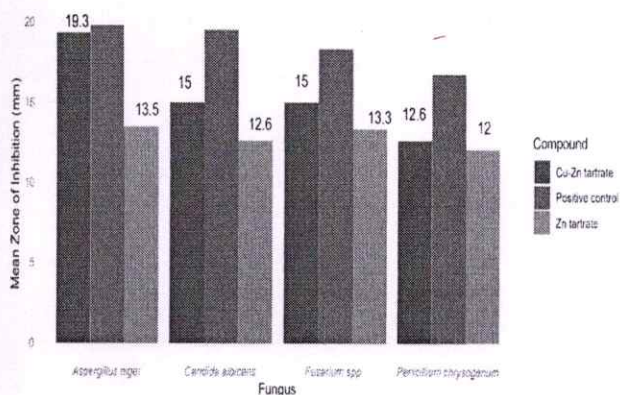

Fig. 14. A bar graph illustrating the diameter of the zone of inhibition (in mm) produced by both ZnT and Cu-ZnT nanocrystals in the presence of fungus.

ZnT. Optical analysis showed strong UV light absorption by both nanocrystals, with high transmittance in the visible and near-infrared regions [45]. Copper doping enhanced the light absorption capacity of Cu-ZnT crystals. The wide bandgaps, confirmed through the analysis, suggest their insulating behavior, valuable for specific applications [46, 47]. Electrical characterization demonstrated a significant increase in
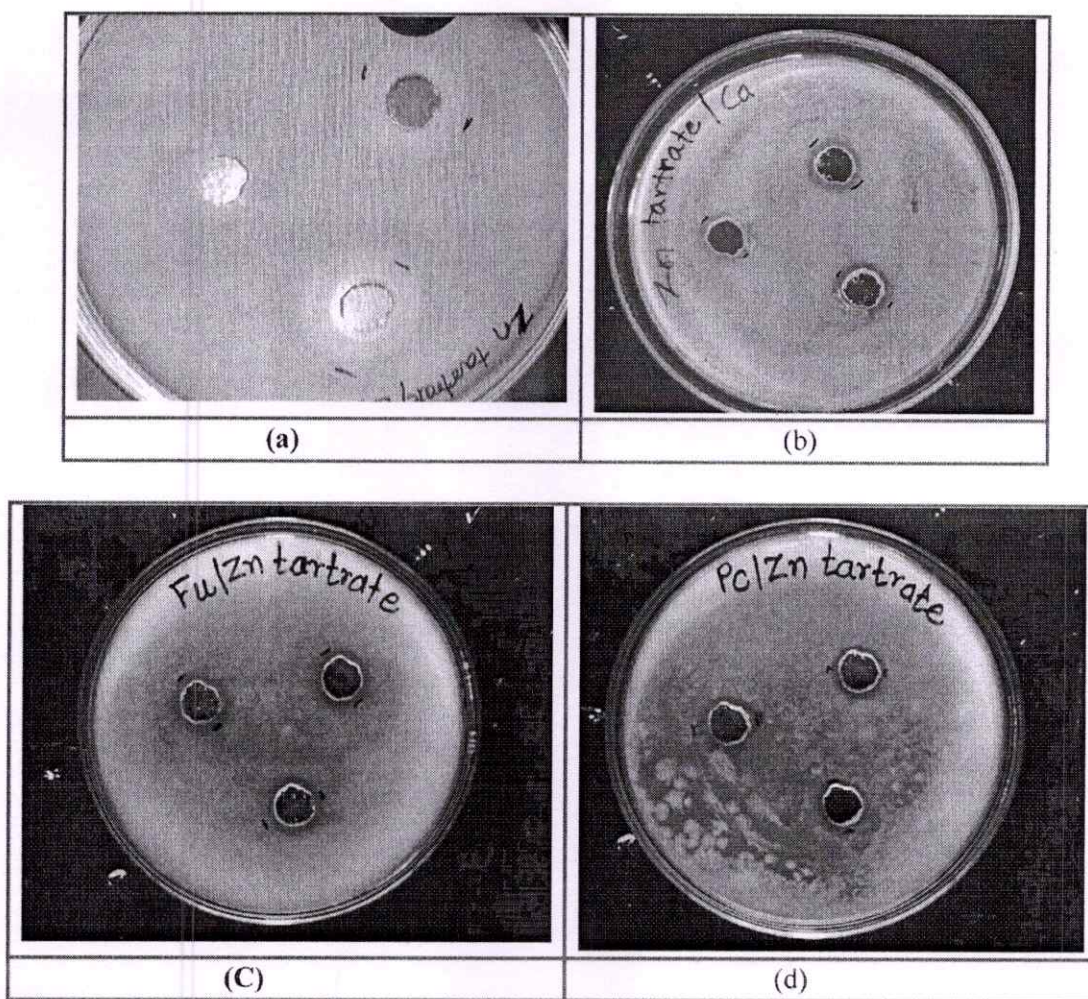

Fig. 13. The zone of inhibition (in mm) produced by both ZnT and Cu-ZnT nanocrystals in the presence of fungus: (a) *Aspergillus Niger*, (b) *Candida albicans*, (c) *Fusarium spp.*, and (d) *Penicillium Chrysogenum*.

conductivity due to copper doping. Cu-ZnT nanocrystals exhibited nearly double the conductivity compared to ZnT. Antimicrobial testing indicated an acceptable level of efficacy against studied bacteria, suggesting potential for further exploration in this area.

Institutional review board statement

Not applicable.

CRediT authorship contribution statement

Madhuri Patil: Writing – review & editing, Writing – original draft, Visualization, Validation, Supervision, Software, Resources. **Charushila Pawar:** Project administration, Methodology, Investigation, Funding acquisition, Formal analysis, Data curation, Conceptualization.

Declaration of Competing Interest

The authors declare that they have no known competing financial interests or personal relationships that could have appeared to influence the work reported in this paper.

Data availability

No data was used for the research described in the article.

References

[1] W. Daoudi, A. Tiwari, M. Tyagi, P. Singh, A. Saxena, D.K. Verma, A. El Aatiaoui, Carbon dots nanoparticles: a promising breakthrough in biosensing, catalysis, biomedical and authers applications, Nano-Struct. Nano-Objects 37 (2024) 101074.

[2] M. Singh, A.K. Keshari, Cd doped ZnO nano-rectangles and their correlation with properties, Nano-Struct. Nano-Objects 38 (2024) 101161.

[3] G. Saxena, I.A. Salmani, M.S. Khan, M.S. Khan, Structural co-related optical properties of Al and Cu co-doped ZnO nanoparticles, Nano-Struct. Nano-Objects 35 (2023) 100986.

[4] B.S. Niveditha, L. Sushmitha, B.K. Usha, G. Nagaraju, Facile green synthesis of Cu-doped MoO3 nanoparticles and its application for the photocatalytic degradation of hazardous organic pollutants, Nano-Struct. Nano-Objects 36 (2023) 101066.

[5] A.M. El Nahrawy, A.S. Montaser, A.M. Bakr, A.B. Abou Hammad, A.M. Mansour, Impact of ZnO on the spectroscopic, mechanical, and UPF properties of Fe 2 O 3-tough polystyrene-based nanocomposites, J. Mater. Sci.: Mater. Electron. 32 (2021) 28019–28031.

[6] S. Singh, M. Joshi, P. Panthari, B. Malhotra, A.C. Kharkwal, H. Kharkwal, Citrulline rich structurally stable zinc oxide nanostructures for superior photo catalytic and optoelectronic applications: a green synthesis approach, Nano-Struct. Nano-Objects 11 (2017) 1–6.

[7] R.S. Feigelson, Crystal growth through the ages: a historical perspective. In. Handbook of Crystal Growth, Elsevier, 2015, pp. 1–83.

[8] J. Govani, M.J. Joshi, Growth and characterization of gel grown potassium hydrogen levotartrate crystals, Indian J. Phys. 82 (2008) 1485–1494.

[9] A.M. El Nahrawy, A.M. Mansour, A.B. Abou Hammad, R.S. Ibrahim, A.M. Abouelnaga, M.S. Abdel-Aziz, Optical, functional impact and antimicrobial of chitosan/phosphosilicate/Al 2 O 3 nanosheets, J. Inorg. Organomet. Polym. Mater. 30 (2020) 3084–3094.

[10] A.M. El Nahrawy, A.B. Abou Hammad, A.M. Mansour, Structural investigation and optical properties of Fe, Al, Si, and Cu-ZnTiO3 nanocrystals. Phys. Scr. 96 (11) (2021) 115801.

[11] A.M. Bakr, A.B.A. Hammad, A.R. Wassel, A.M.E. Nahrawy, A.M. Mansour, Influence of Al, Fe, and Cu on the microstructure, diffused reflectance, THz, and dielectric properties for ZnTiO3 nanocrystalline, Int. J. Mater. Eng. Innov. 12 (2) (2021) 115–133.

[12] A.M. El Nahrawy, A.B.A. Hammad, A.M. Youssef, A.M. Mansour, A.M. Othman, Thermal, dielectric and antimicrobial properties of polystyrene-assisted/TiO2-Cu nanocomposites, Appl. Phys. A 125 (2019) 1–9.

[13] A.M. Mansour, Thermal microscopy (TM), Int. J. Microstruct. Mater. Prop. 15 (3) (2020) 215–228.

[14] M. Moradi, M. Abdolhosseini, A. Zarrabi, A review on application of nano-structures and nano-objects with high potential for managing different aspects of bone malignancies, Nano-Struct. Nano-Objects 19 (2019) 100348.

[15] K.V. Pradeepkumar, N. Jagannatha, P.S. Rohith, Effect of semiconductor laser irradiation on growth and characterization of cadmium doped copper tartrate single crystals, J. Cryst. Growth 563 (2021) 126107.

[16] K. Sharma, A.S. Al-Kabbi, G.S.S. Saini, S.K. Tripathi, Effect of Cu incorporation on structural and optical properties of nanocrystalline CdSe (nc-CdSe: Cu) thin films, J. Alloy. Compd. 540 (2012) 198–203.

[17] A.M. El Nahrawy, A.B. Abou Hammad, A.M. Mansour, Structural investigation and optical properties of Fe, Al, Si, and Cu-ZnTiO3 nanocrystals, Phys. Scr. 96 (11) (2021) 115801.

[18] K. Suryanarayana, S.M. Dharmaprakash, Crystal growth and characterization of barium doped calcium tartrate tetrahydrate crystals, Mater. Lett. 42 (1-2) (2000) 92–96.

[19] A.A. Azab, A.M. Mansour, G.M. Turky, Structural, magnetic, and dielectric properties of Sr4Fe6O13 ferrite prepared of small crystallites, Sci. Rep. 10 (1) (2020) 4955.

[20] G.S. David, S. Revathi, M.B.J. Raj, Structural and optical characterisation of zinc doped potassium hydrogen tartrate crystal for antibacterial analysis, Sch. J. Eng. Technol. 2 (2014) 795–802.

[21] K.B. Reema, N. Jagannatha, K.P. Nagaraja, D. D'Souza, Magnesium and zinc diffused growth and characterization of strontium L (+) tartrate pentahydrate crystals, J. Adv. Appl. Sci. Res. 3 (1) (2021) 7–15.

[22] M. Mani, S. Pavithra, K. Mohanraj, S. kumaresan, S.S. Alotaibi, M.M. Eraqi, K. Kaviyarasu, Studies on the spectrometric analysis of metallic silver nanoparticles (Ag NPs) using Basella alba leaf for the antibacterial activities, Environ. Res. 199 (2021) 111274.

[23] A. Dakka, J. Lafait, C. Sella, S. Berthier, M. Abd-Lefdil, J.C. Martin, M. Maaza, Optical properties of Ag-TiO 2 nanocermet films prepared by cosputtering and multilayer deposition techniques, Appl. Opt. 39 (16) (2000) 2745–2753.

[24] J.K. Kana, J.M. Ndjaka, B.D. Ngom, N. Manyala, O. Nemraoui, A.Y. Fasasi, M. Maaza, Thermochromic nanocrystalline Au-VO2 composite thin films prepared by radiofrequency inverted cylindrical magnetron sputtering, Thin Solid Films 518 (6) (2010) 1641–1647.

[25] G.G. Welegergs, H.G. Gebretinsae, M.G. Tsegay, A. Bhardwaj, S. Mathur, T. G. Kebede, M. Maaza, Spectrally selective single layered Ag@ CuO nanocermet coatings for photothermal application: green synthesis method, Opt. Mater. 135 (2023) 113247.

[26] A.K. Patil, U.S. Jagtap, H.R. Talele, Growth and characterization of zinc tartrate crystals in agar-agar gel, Int. J. Basic Appl. Sci. 11 (2022) 86–90.

[27] J. Chen, J. Si, A. Pal, Y. Gao, Y. Zhang, Y. Chen, Z. Feng, Evidence of superconductivity induced by copper doping in Nb1e2 single crystals, J. Supercond. Nov. Magn. 36 (4) (2023) 1103–1108.

[28] Y. Liu, T. Lin, R. Huang, J. Shi, S. Chen, Analysis of the effect of copper doping on the optoelectronic properties of indium oxide thin films and the thermoelectric properties of an In2O3/Pt thermocouple, Crystals 14 (1) (2024) 78.

[29] F. Zhao, S. Hu, C. Xu, H. Xiao, X. Zhou, X. Zu, S. Peng, Effect of copper doping on electronic structure and optical absorption of Cd3Se3 quantum dots, Nanomaterials 11 (10) (2021) 2531.

[30] S. Tavakoli, M. Kharazha, S. Nemati, Polydopamine coated ZnO rod-shaped nanoparticles with noticeable biocompatibility, hemostatic and antibacterial activity, Nano-Struct. Nano-Objects 25 (2021) 100639.

[31] B.K. Mohammed, M.K. Mohammed, D.S. Ahmed, The effect of copper doping on the structural, optical, and electrical properties of nickel oxide thin films for optoelectronic applications, J. Sol. Gel Sci. Technol. 99 (2021) 1–12.

[32] P. kolandaivel, S. Selvasekarapandian, FT-IR and Raman spectra of ammonium hydrogen tartrate and potassium hydrogen tartrate crystals, Cryst. Res. Technol. 28 (5) (1993) 665–670.

[33] A.M. El Nahrawy, B.A. Hemdan, A.B. Abou Hammad, A.M. Othman, A. M. Mansour, Modern template design and biological evaluation of cephradine-loaded magnesium calcium silicate nanocomposites as an inhibitor for nosocomial bacteria in biomedical applications, Silicon 13 (2021) 2979–2991.

[34] V. Mathivanan, M. Haris, T. Prasanyaa, M. Amgalan, M. Senthilkumar, Structural, magnetic, dielectric and thermal analysis of gel grown pure and doped cadmium tartrate crystals, Optik 125 (18) (2014) 5153–5159.

[35] R.S. Ibrahim, A.A. Azab, A.M. Mansour, Synthesis and structural, optical, and magnetic properties of Mn-doped CdS quantum dots prepared by chemical precipitation method, J. Mater. Sci.: Mater. Electron. 32 (14) (2021) 19980–19990.

[36] X.H. Li, Y.X. Guo, Y. Ren, J.J. Peng, J.S. Liu, C. Wang, H. Zhang, Narrow-bandgap materials for optoelectronics applications, Front. Phys. 17 (2022) 1–33.

[37] H.E.A. Mohamed, A.T. Khalil, K. Hkiri, M. Ayaz, A. Usman, A. Sadiq, M. Maaza, Structural, vibrational, optical, and anticancer properties of Hyphaene thebaica-reduced nano-lanthanum oxide (La2O3), Appl. Organomet. Chem. 37 (6) (2023) e7091.

[38] G.A. Kaningini, S. Azizi, H. Nyoni, F.N. Mudau, K.C. Mohale, M. Maaza, Green synthesis and characterization of zinc oxide nanoparticles using bush tea (Athrixia phylicoides DC) natural extract: assessment of the synthesis process, F1000Research 10 (2021).

[39] G.G. Welegergs, H.G. Gebretinsae, M.G. Tsegay, A. Bhardwaj, S. Mathur, T. G. Kebede, M. Maaza, Spectrally selective single layered Ag@ CuO nanocermet coatings for photothermal application: green synthesis method, Opt. Mater. 135 (2023) 113247.

[40] D. Havenga, R. Akoba, L. Menzi, S. Azizi, J. Sackey, N. Swanepoel, M. Maaza, From Himba indigenous knowledge to engineered Fe2O3 UV-blocking green nanocosmetics, Sci. Rep. 12 (1) (2022) 2259.

[41] A.K. Patil, U.S. Jagtap, H.R. Talele, Growth and characterization of zinc tartrate crystals in agar-agar gel, Int. J. Basic Appl. Sci. 11 (2022) 86–90.

[42] N. Madubuonu, S.O. Aisida, A. Ali, I. Ahmad, T.K. Zhao, S. Botha, F.I. Ezema, Biosynthesis of iron oxide nanoparticles via a composite of Psidium guavaja-Moringa oleifera and their antibacterial and photocatalytic study, J. Photochem. Photobiol. B: Biol. 199 (2019) 111601.

[43] **Bioreduction potentials of dried root of Zingiber officinale for a simple green synthesis of silver nanoparticles: antibacterial studies, JJ Vijaya, N Jayaprakash, K**

Kombaiah, K Kaviyarasu, LJ Kennedy,Journal of Photochemistry and Photobiology B: Biology 177, 62-68(2017).

[44] N. Madubuonu, S.O. Aisida, I. Ahmad, S. Botha, T.K. Zhao, M. Maaza, F.I. Ezema, Bio-inspired iron oxide nanoparticles using Psidium guajava aqueous extract for antibacterial activity, Appl. Phys. A 126 (2020) 1–8.

[45] A.M. Mansour, I.M.E. Radaf, T.A. Hameed, G.B. Sakr, Investigation of ag2hgi4 nanoparticles: thermal phase transition and non-isothermal kinetic study, UPB Sci. Bull., Ser. B: Chem. Mater. Sci. 81 (1) (2019) 134–148.

[46] E.M. El-Menyawy, I.T. Zedan, A.M. Mansour, H.H. Nawar, Thermal stability, AC electrical conductivity and dielectric properties of N-(5-([antipyrinyl-hydrazono]-cyanomethyl)-[1, 3, 4] thiadiazol-2-yl]-benzamide, J. Alloy. Compd. 611 (2014) 50–56.

[47] E.M. El-Menyawy, A.M. Mansour, N.A. El-Ghamaz, S.A. El-Khodary, Electrical conduction mechanisms and thermal properties of 2-(2, 3-dihydro-1, 5-dimethyl-3-oxo-2-phenyl-1H-pyrazol-4-ylimino)-2-(4-nitrophenyl) acetonitrile, Phys. B: Condens. Matter 413 (2013) 31–35.